Journal of Civil Engineering and Management
ISSN 1392-3730 / eISSN 1822-3605
2022 Volume 28 Issue 7: 523–535
https://doi.org/10.3846/jcem.2022.16683

INVESTIGATION OF THE PERFORMANCE OF RC BEAMS REINFORCED WITH FRP AND ECC MATERIALS

Guorui SUN[1,2], Jie LAI[3], Yuzhou ZHENG[4], Kaikai ZHENG[2], Jun SHI[1,5*]

[1]*School of Civil Engineering, Central South University, Changsha, China*
[2]*Key Lab of Structures Dynamic Behavior and Control of the Ministry of Education, Harbin Institute of Technology, Harbin, China*
[3]*Academy of Combat Support, Rocket Force University of Engineering, Xi'an, China*
[4]*School of Field Engineering, Army Engineering University of PLA, Nanjing, China*
[5]*National Engineering Laboratory for High Speed Railway Construction, Changsha, China*

Received 15 October 2021; accepted 18 January 2022

Abstract. This paper investigates the structural working behavior of reinforced concrete beams bonded with fiber reinforced polymer and engineered cementitious composite materials subjected to bending using structural stressing state theory. First, six reinforced concrete beams externally bonded with composite reinforcement layer and one control beam are tested to investigate the effects of the bond length, fiber reinforced polymer grid thickness and fiber content on the flexural behavior. Then, the finite strain data of RC beams are interpolated by the numerical shape function method. The generalized strain energy density model is established to characterize the stressing state of the structure. Through the Mann-Kendall criterion, the characteristics load P and Q of the beams are detected, and the whole loading process is divided into three stage. Finally, the analysis of the strain and deformation on the beams reveals the effect of different parameters on different stage. The characteristic load P increases as the bond length increases, and the characteristic load Q increases as the thickness of the FRP and the fiber content increase. The vertical deformation of the strengthened beam for the characteristic load Q and ultimate load is significantly smaller than that of the unreinforced beam.

Keywords: fiber reinforced polymer, composite reinforcement layer, stressing state, characteristic load, reinforcement concrete beam.

Introduction

Over the past few decades, the demand for repairing and strengthening reinforced concrete (RC) structures has steadily increased. Among them, fiber reinforced polymer (FRP) has been widely used in the repair and reinforcement of RC beams due to its convenient construction, light weight and high strength (Godat et al., 2020; He et al., 2020; Sogut et al., 2021).

In recent years, many valuable experimental studies have been carried out to investigate the working behavior of beams strengthened with FRP. The curvature, deflection and flexural performance of RC beams determined using different reinforcement methods were compared through experimental and theoretical analyses. The results show that the bearing capacity of RC beams strengthened with the FRP method is better than that achieved by other reinforcement methods (Li et al., 2020). In a corrosive environment, the bearing capacity of an FRP-reinforced beam is also significantly improved. In the case of steel corrosion, the ultimate load of an FRP-reinforced beam was 14.8% higher than that of the unreinforced beam (Kadhim et al., 2019). The reason for this may be that the FRP plays an important role in resisting the load after the reinforcement yields (Kara et al., 2015). The bonding property between FRP and concrete is the key factor for controlling the behavior of RC structures strengthened with FRP (Yao et al., 2005). However, traditional bonding materials, such as epoxy resins, are susceptible to environmental effects. Therefore, many scholars have attempted to utilize other innovative bonding materials to replace epoxy resins and update the FRP strengthening system (Al-Salloum et al., 2011; Dai et al., 2014; Escrig et al., 2015; Ge et al., 2017).

*Corresponding author. E-mail: *csushijun@csu.edu.cn*

Engineered cementitious composite (ECC) materials with high ductility and multipoint uniform cracking have a wide range of applications in civil engineering (Ma et al., 2021; Shanmugasundaram & Praveenkumar, 2021). When FRP and ECC materials are combined to reinforce a structure, the properties of both can be effectively utilized, and the ultimate load of the structure can be significantly increased. Hence, researchers have used ECC materials as the transition layer to investigate the flexural behaviors of RC beams strengthened with FRP (Afefy et al., 2015; Yuan et al., 2021). The results show that ECC materials could avoid the premature shedding of FRP sheets and improve the ultimate load of the test beams. Ge et al. investigated the effect of the FRP content and ECC thickness on the flexural properties of RC beams. Based on the test results, the failure modes of the strengthened beams were determined, and a formula for calculating the bearing capacity was proposed (Ge et al., 2019). Zheng et al. proposed a new strengthening method for RC beams by combining basalt FRP grid and ECC materials as a composite reinforcement layer (CRL). The proposed technique is effective for suppressing the debonding of externally bonded materials and fully utilizing the strength of the material (Zheng & Wang, 2015; Zheng et al., 2016, 2018).

In summary, a great deal of research has been conducted on strengthening RC structures with FRP. However, there are still two problems to be solved in the analysis of structures strengthened with FRP and ECC materials, which are summarized below:

1. The reliability of the reinforced system must still be verified due to the limited experimental data. At the same time, the existing analytical methods cannot effectively investigate the stressing state characteristics of the structure, and the limited experimental test data cannot be fully exploited.
2. Researchers have concentrated on studying the increase in the ultimate load of beams rather than clarifying the effects of the reinforcement methods on the different loading stages. The effect of different parameters on the flexural properties of the structure at different loading stages is not clear.

In view of the above problems, this paper investigates the working behavior of RC beams strengthened with a CRL through the bending test. Based on the numerical shape function (NSF) method, the limited strain data of the beams are interpolated to obtain more detailed strain information. Then, through structural stressing state theory, the generalized strain energy density (GSED) model is introduced to analyze the stressing state of the structure. The leap characteristic in the $E_{j,norm}$-F_j curve can be detected by the Mann-Kendall (M-K) criterion, and the loading stages of the structure can be divided through the characteristic load. In addition, according to the strain mode and the deformation of the experimental beams, the reliability of the characteristic load is verified. Finally, the influence of different parameters on the structure at different loading stages can be determined by comparing the characteristic load, section strain and displacement.

1. Experiments for RC beams strengthened with CRL

1.1. Configuration of the experimental RC beams

The flexural experiment was performed on RC beams strengthened with an FRP grid and an ECC Southeast University, and the dimensions of the structure are shown in Figure 1. The experimental RC beam was 1800 mm in length, 200 mm in width and 300 mm in height. The effective length of the beam was 1700 mm with two ends simply supported. The yield stress and fracture strength of the longitudinal reinforcement were 560 MPa and 640 MPa, respectively. And the compressive strengths of concrete were 35 MPa. After the RC beams were maintained for 28 days and polished with a grinding wheel, the BFRP grid was first fixed to the bottom surface of the RC beams by means of pre-built steel studs. After that, a 30 mm thick ECC layer was placed along the longitudinal direction of the beam to form the CRL. The CRL is located below the beam with a width of 200 mm. The CRL was fabricated into a plate with dimensions of 400 mm (length) × 100 mm (width) × 30 mm (thickness) for the tensile test. The ultimate loads of CRL for 0 mm, 1 mm, 3 mm and 5 mm thick BFRP grids were 8.5 kN, 12 kN, 16.8 kN and 20.1 kN, respectively. No relative slip occurred between FRP and ECC, while the damage mode of CRL was FRP fracture damage. The properties of FRP and ECC in CRL are shown in Table 1 to Table 3.

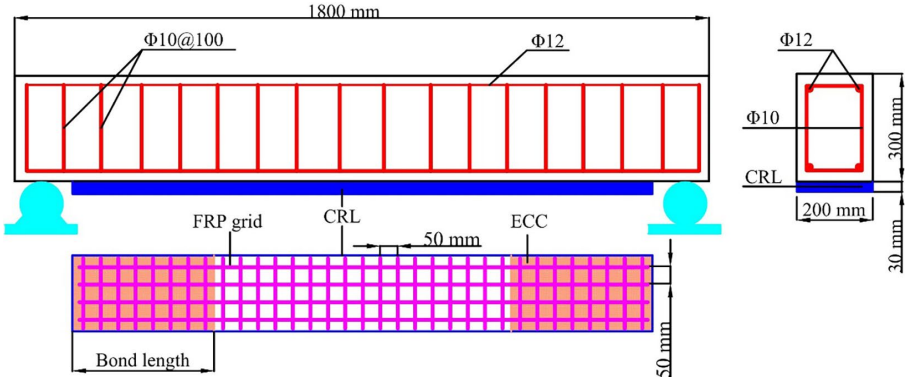

Figure 1. Structural dimensions of the experimental RC beam

Table 1. Properties of ECC

Water (kg/m^3)	Cement (kg/m^3)	Flay ash (kg/m^3)	Quartz sand (kg/m^3)	Silica fume (kg/m^3)	Water reducer (kg/m^3)	PVA fiber (%)
1.4	1	4	0.15	0.15	0.05	1.3/2.0

Table 2. Properties of FRP

Thickness of FRP grid (mm)	Tensile strength of FRP (MPa)	Elongation (%)	Modulus of elasticity (GPa)
1	357	0.27	51
3	386	0.26	53
5	416	0.22	57

Table 3. Different factors of the experimental RC beams

Number	Bond length of CRL (mm)	Fiber content of ECC (%)	Thickness of FRP grid (mm)	Compressive strength of ECC (MPa)
BB0	None	None	None	None
BB1	500	1.3	1	31
BB2	500	1.3	3	31
BB3	500	1.3	5	31
BB4	450	1.3	3	31
BB5	400	1.3	3	31
BB6	500	2.0	3	33

1.2. Distribution of the measurement points and loading scheme

Figure 2a shows the distribution of the displacements and strain measurement points of the experimental beams. The strains of the longitudinal reinforcement were recorded in the mid-span cross section, the loading cross section and the bearing cross section. The strains of the concrete, CRL and FRP grid were recorded in the mid-span cross section. Among them, G1–G5 represent the strain of the concrete, and G6 represents the strain of the CRL. G7, G9 and G10 represent the strain of the steel bar at different cross sections. G8 represents the strain of the FRP grid. The displacements were recorded in the mid-span cross section and the loading cross section through the displacement meter. The distance between the mid-span cross section and the loading cross section was 250 mm.

During the test, four-point bending tests were used for all beams. First, the concentrated load was applied through the jack at the top of the experimental setup, and then the concentrated load was distributed to two loading points through the distributed beam, as shown in Figure 2b. The distance between the loaded section and the center section of the span was 250 mm. The loads were applied in a step-by-step approach, each step was held for 5 minutes and the deformation and crack development of the beams were recorded. The magnitude of the concentrated load was recorded by a loading sensor connected to a hydraulic jack. The increment of the concentrated load was fixed at 5 kN/ grade before the concrete crack and 10 kN/ grade after the concrete crack. When the experimental beam was broken, the test ended and the damage model was recorded.

2. Theoretical analysis method

2.1. Numerical shape function method

In structural analysis, the experimental data can characterize the working behavior of a structure to some extent, but the response mechanism and characteristics of the structure cannot be fully presented due to a limitation in the measuring instrument. Hence, to obtain more information regarding the response mechanism and characteristics of the structure, the NSF method was proposed, which can accurately interpolate or extend experimental data with clear physical significance. The NSF method is a new and effective interpolation method that directly interpolates experimental data fields through traditional shape functions and finite element simulations. This approach not only overcomes the disadvantages of traditional shape functions but also meets the accuracy requirements of experimental analysis.

To vividly introduce the NSF method, the strain field of the experimental beam numbered BB5 is taken as an example. As shown in Figure 3a, the mid-span cross section

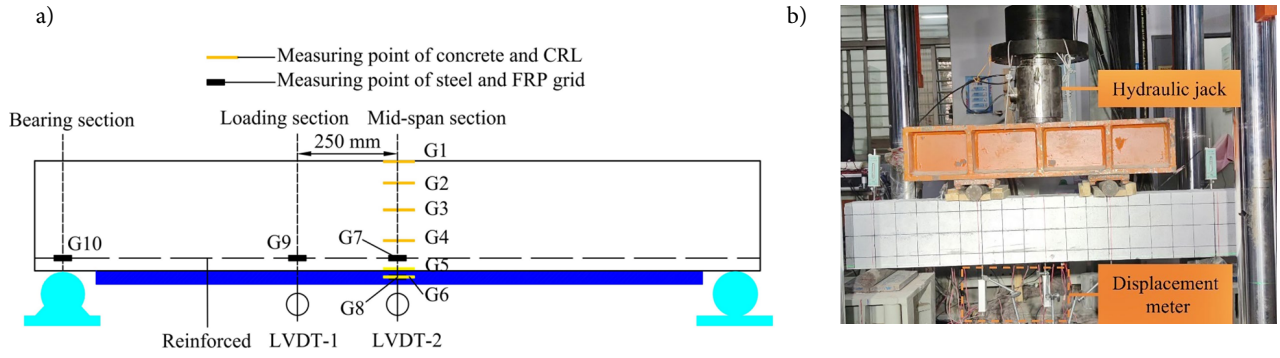

Figure 2. Experimental device: a – Distribution of the strain and displacement measurement points of the RC experimental beams; b – Loading scheme of the RC experimental beam

was constructed by using ANSYS software. Shell unit 181 was used for the concrete slab and CRL slab with a thickness of 5 mm, and the unit area was 5×5 square mm. The beam 188 elements were used to simulate ordinary steel rebar and FRP in the cross-section. Its thickness was also 5 mm, and their area was the actual area. Additionally, it was assumed that the connection between the steel bar and the concrete is was rigid. Moreover, 16 measurement nodes in the mid-span cross section were taken as the basic nodes of the numerical shape function. By applying displacement at the *i*-th measuring nodes and limiting displacement at other measurement nodes, the shape function $\mathbf{N}_i$ of the measuring nodes *i* can be obtained from the finite element simulation, such as $\mathbf{N}_3$ and $\mathbf{N}_9$ shown in Figure 3b and 3c.

Without considering large deformation and elasto-plasticity, the simulation results calculated by this method can be superimposed linearly. Therefore, the NSF method can be used to calculate the interpolation field of the mid-span cross section of the experimental beam as follows:

$$\mathbf{N}_i = \left[N_i(x_1), N_i(x_2) \cdots N_i(x_j) \cdots N_i(x_n) \right], \quad (1)$$

where $\mathbf{N}_i$ is the numerical shape function of the *i*-th measuring node, $N_i(x_j)$ is the simulated value at element node x_j and *n* is the total node of the plate.

$$\mathbf{D} = \sum_{i=1}^{m} u_i \mathbf{N}_i, \quad (2)$$

where **D** is the deflection field of the section, u_i represents the measuring samples and *m* is the total number of measured nodes. Among them, there is no CRL section of the experimental beam BB0. Therefore, *m* = 12 when the experimental beam is BB0, and *m* = 16 when referring to the other experimental beams.

Accordingly, the finite measured strain in the cross section can be interpolated by shape function expansion to obtain the strain field. To verify the precision of the NSF method, 14 out of 16 measured strain nodes on the mid-span cross section are adopted to construct the strain field, and then the interpolation results at the other two points can be obtained. These values are compared with

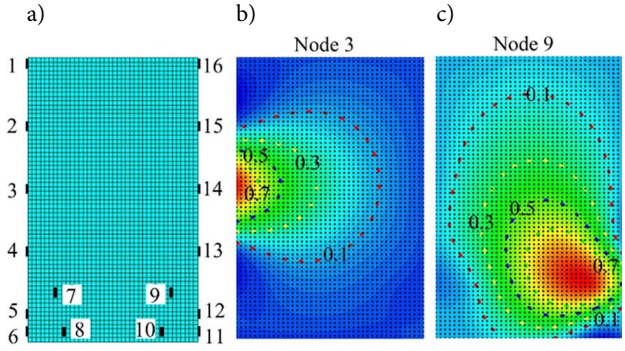

Figure 3. Finite element model: a – Measuring point; b – Node 3; c – Node 9

the real measured values, and the error between them can be calculated by Eqn (3):

$$\delta_{ij} = \left| \frac{\varepsilon_{ij}^{s} - \varepsilon_{ij}^{e}}{\varepsilon_{ij}^{e}} \times 100\% \right|, \quad (3)$$

where δ_{ij} is the error of the *i*-th node at the *j*-th load step between the interpolation and experiment and εs *ij* and εe *ij* are the interpolating and experimental strains of the *i*-th node at the *j*-th load step, respectively. The average error of the *i*-th node in the whole loading process can be estimated by Eqn (4):

$$\overline{\delta}_i = \frac{1}{N} \sum_{j}^{N} \delta_{ij}, \quad (4)$$

where $\overline{\delta}_i$ is the average error of the *i*-th node and *N* is the total number of load steps. Hence, the precision of the NSF method can be determined through the error values and the comparison curves comparing the interpolated and experimental data.

Taking measuring nodes 2 and 13 as examples, the experimental and interpolation curves of the measuring points are shown in Figure 4a, and the fitting degree of the data can be clearly observed. During the entire loading process, the curves for the same point have very high fitting degrees. The error of all measuring points is shown in Figure 4b, and the error results are relatively small, and

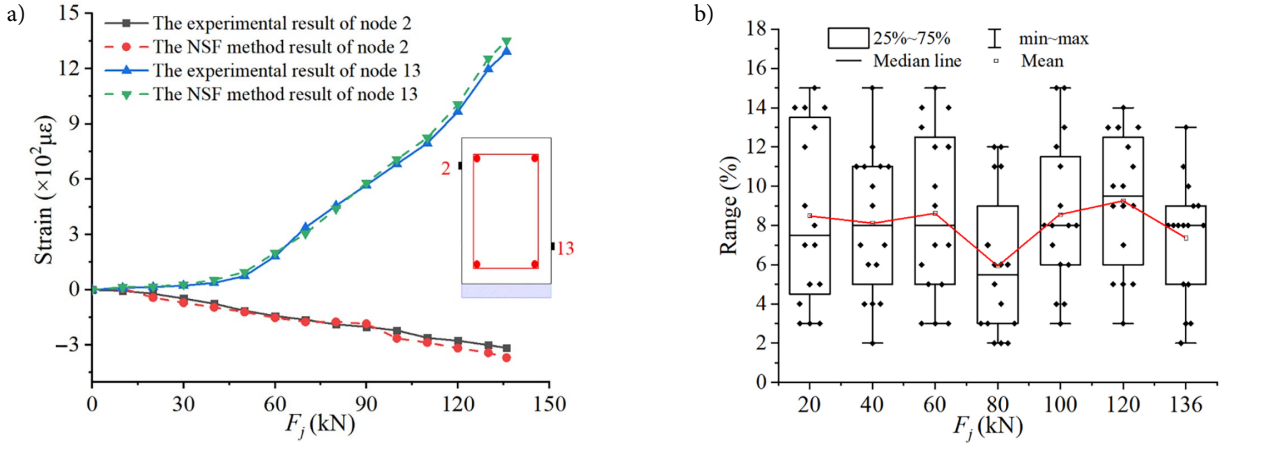

Figure 4. The error results of strain data mid-span section: a – Comparison curve of measuring points in mid-span section; b – Error of all measuring points

the average errors are less than 9% and the maximum errors are less than 15% throughout the loading period, thus fully meeting the application requirements. Therefore, the NSF method can be used to sufficiently and accurately extend the experimental data to explore the potential characteristics of the structural forces in depth.

The working behavior and failure mechanism of the structure can be investigated more comprehensively through the changing characteristics of the internal forces. Therefore, the in-plane bending moment of the mid-span cross section can be constructed by the NSF method. The calculation method of the in-plane bending moment was achieved by summing the product of the longitudinal stress, vertical distances and area for each element:

$$M_j = \int_A \sigma y \mathrm{d}A = \sum_A \sigma_{ij} y_i A_i \,, \tag{5}$$

where σ_{ij} is the stress of the i-th element at the j-th load step, A_i is the area of the i-th element, M_j is the in-plane bending moment at the j-th load step, and y_i is the vertical distance of the i-th element from the neutral axis.

2.2. Structural stressing state concept

To resolve the problem that the definition of the structural stressing state is not uniform and accurate, this paper defines the stressing state of the loaded structure as the structural working behavior. In other words, the stressing state of the structure is defined as the internal or external mode of the structure under a certain load, which is characterized by the numerical model of the structural responses such as strains, displacements, and GSEDs. The stressing state of the structure will change with increasing load, showing different characteristics at certain load levels, which is in accordance with the law of the quantitative to qualitative change of the system. To determine the corresponding numerical model and characteristic parameters of the structure, the GSED is introduced to express the stressing state of the measured point (Huang et al., 2014; Mann, 1945). Hence, the GSED can be calculated by Eqn (6):

$$E_{ij} = \int_0^{\varepsilon_{ij}} \sigma \mathrm{d}\varepsilon, \tag{6}$$

where E_{ij} is the GSED value of the i-th measured point under the j-th load and ε_{ij} is the strain value of the i-th point under the j-th load. The strain of every node on the cross section is obtained through the NSF method, and the GSED values can be summed by Eqn (7):

$$E_j = \sum_{i=1}^{N} E_{ij} A_i \,, \tag{7}$$

where E_j is the GSED value of the measured section at the j-th load step; N is the number of elements; and A_i is the area of the i-th element. Then, a normalized GSED value is adopted as a characteristic parameter of the structural stressing state, and the normalized GSED sum is calculated by Eqn (8):

$$E_{j,norm} = \frac{\sum_{i=1}^{N} E_{ij}}{E_M}, \tag{8}$$

where $E_{j,norm}$ is the normalized GSED sum under the j-th load; E_M is the maximum strain energy value over the loading process; and N is the total number of measured points. Thus, the structural stressing state could be appropriately characterized by the GSED values, and the $E_{j,norm}$ -F_j curve of the structure could be plotted to investigate the stressing state characteristics of the structure.

2.3. M-K criterion

The M-K criterion is a widely used trend analysis tool that does not need to comply with a certain distribution or adapt to the interference of individual outliers (Kendall & Gibbons, 1990; Shi et al., 2019; Xiao et al., 2021). Hence, the M-K criterion is applied to identify the mutation of the structural stressing state from the $E_{j,norm}$-F_j curve. It is assumed that the sequence of $E_{j,norm}$ (the j-th load step, where j is 1, 2, …, n) is statistically independent. Then, the M-K criterion procedure is as follows:

For the $E_{j,norm}$-F_j curve, the cumulative number m_i and stochastic variable d_k are calculated by the following equations:

$$m_i = \begin{cases} +1 & E_{j,norm}(i) > E_{j,norm}(j)\left(1 \le j \le i\right) \\ 0 & \text{otherwise} \end{cases}; \tag{9}$$

$$d_k = \sum_{i}^{k} m_i \left(2 \le k \le n\right). \tag{10}$$

The "+1" value means adding one more to the existing value if the inequality on the right side is satisfied for the j-th comparison. The mean value $E(d_k)$ and the variance $V(d_k)$ of d_k can be calculated by the following equations:

$$E\left(d_k\right) = \frac{k\left(k-1\right)}{4}\left(2 \le k \le n\right); \tag{11}$$

$$V\left(d_k\right) = \frac{k\left(k-1\right)\left(2k+5\right)}{72}\left(2 \le k \le n\right). \tag{12}$$

By normalizing d_k, the gradient UF_k can be calculated by Eqn (13):

$$UF_k = \frac{\left(d_k - E(d_k)\right)}{\sqrt{v(d_k)}}. \tag{13}$$

Finally, the UF_k-F curve can be plotted. The proceeding inverse E' sequence is consistent with the prior sequence, which can form the UB_k -F curve. Therefore, the leap points of the $E_{j,norm}$ -F_j curve can be determined by the intersection of the UF_k and UB_k curves.

3. Analysis of experimental results

3.1. Ultimate loads and failure modes

For beam BB0, the concrete at the bottom cracked when the load was 31 kN. With increasing load, the cracks continued to expand along the height direction of the beam,

while the number of microcracks at the bottom continued to increase. After the reinforcement yielded, the deformation of the structure increased rapidly. With a further increase in load, the concrete in the compression zone was damaged. For beams BB1~BB6, when the load was 51~61 kN, the concrete at the bottom cracked, while multiple microcracks appeared in the CRL. As the load increased, the width and number of cracks at the bottom increased, and the number of microcracks extended toward the loading point. After the reinforcement yielded, the CRL showed multipoint uniform cracking. Microcracks started to appear at the interface between the CRL and concrete for beams BB3 and BB6. With the further increase in load, the FRP of the beams fractured, and the structure reached the ultimate load.

The ultimate loads and damage modes of the specimens are shown in Figure 5. The damage mode of RC beam BB0 in the control group is concrete crushing after yielding of the reinforcement. The damage mode of RC beam BB0 in the control group is concrete crushing after yielding of the reinforcement. The damage modes of beams BB1, BB2, BB4 and BB5 are that the FRP fractures first, and then, the concrete is crushed in the compressed area. The damage mode of beam BB3 is first FRP fracture, and then, the interface between the CRL and concrete is separated and damaged. The damage mode of test beam BB6 is that the FRP fractures first, then partial separation between the CRL and concrete occurs, and finally, the concrete in the compression zone is crushed. The bond length of the CRL does not change the damage mode of the beam. The results show that with the increase in the fiber content in the ECC and the thickness of the FRP, the damage pattern changes, and separation of the CRL and concrete interface may occur. The bond length of the CRL does not change the damage mode of the beam. Comparing the ultimate loads of different beams shows that the ultimate loads of RC beams keep increasing as the thickness of the FRP grid, the fiber content of the ECC and the bond length of the CRL increase.

3.2. Investigation into the $E_{j,norm}$-F_j curve

In order to study the effect of each influencing factor on the beam at each stage of the loading process after strengthening, the structural stressing state theory and NSF method are used to study the sudden change characteristics of the structure. The stressing state model of the RC beam is represented by the GSED value composed of the strain data, which can be calculated from Eqn (6). The $E_{j,norm}$-F_j curve can be described to investigate the developing tendency and sensitivity of the RC beam's stressing state during the entire loading process.

In this section, taking the experimental beam BB5 as an example, the $E_{j,norm}$-F_j curve is plotted to analyze the working behavior of the RC beam, as shown in Figure 6. Characteristic load P (50 kN) and characteristic load Q (110 kN) in the $E_{j,norm}$-F_j curve are distinguished by the M-K criterion. Before characteristic load P is reached, the curve increases slowly and approaches a straight line, indicating that the experimental beam is in a stable stressing state. After that, the curve still increases slowly, but the growth rate increases and is curvilinear, indicating that the test beam undergoes some plastic deformation and the stressing state of the structure changes. Beyond characteristic load Q, the curve increases sharply compared with the previous stage, displaying a different tendency, indicating that the RC beam changes from a stable stressing state to an unstable stressing state.

In conclusion, characteristic load P can be regarded as the demarcation point of the RC beam from one working state to another. At this time, although the working state changes, the whole structure remains in a stable working state. The working state of the structure changes qualitatively beyond characteristic load Q and is different from the working state of the previous stage. The RC beam can be seen as the demarcation point from a stable working state to structural failure. Characteristic load Q is different from the ultimate load and is the starting point of the structure failure process.

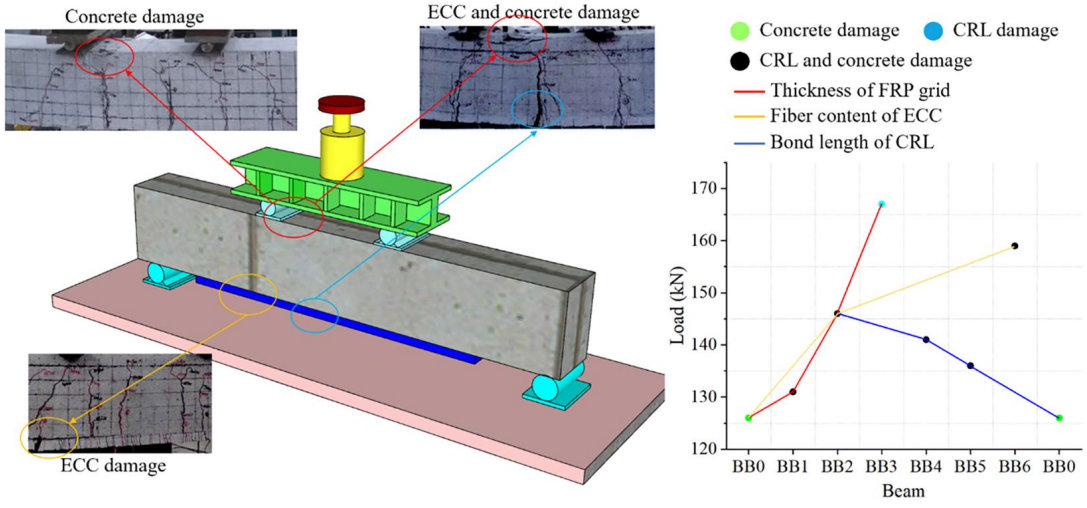

Figure 5. Ultimate loads and failure modes

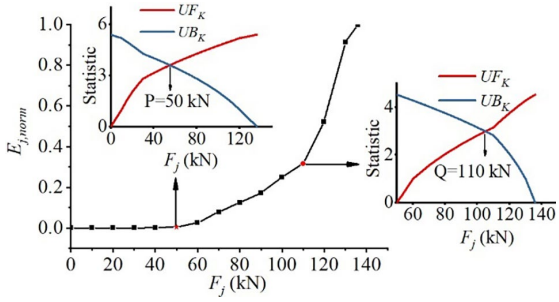

Figure 6. The $E_{j,norm}$-F_j curve and M-K statistic curves of the experimental RC beam numbered BB5

3.3. Investigation into the characteristics of the strain fields

The mid-span cross section of the experimental beam is meshed through the finite element method, and the measured strain is interpolated according to the NSF method to obtain the strain field. The strain contour map near the characteristic loads P and Q was analyzed, as shown in Figure 7. To analyze the strain distribution of the mid-span cross section, dotted lines of different colors are used to represent the different strain values. Among them, the separatrix of 0 με is marked with a red dotted line to identify the distributions of the compression zone and tension zone of concrete. The ultimate tensile strain of the concrete is marked with a black dotted line to show the working condition of the concrete.

At the beginning of loading, the strain of the mid-span cross section is small, and the distribution is uniform, as shown in Figure 7a. The strain of concrete is less than the ultimate tensile strain, indicating that the stressing state of concrete does not change. When the load reaches 50 kN (characteristic load P), the region beyond the ultimate tensile strain appears and expands with an increase in the load. At the same time, the strain of the longitudinal reinforcement and FRP grid increases rapidly, and the maximum tensile strain of the mid-span cross section is concentrated in the CRL and reinforcement region. As shown in Figure 7b, beyond characteristic load Q, the maximum tensile strain of the mid-span cross section is concentrated in the CRL region. Compared with the previous stage, the gap between the strain of the FRP grid and the strain of the reinforcement increases rapidly, indicating that the tensile strain is mainly borne by the FRP grid during the failure stage. The strain distribution of the CRL in beam BB5 is relatively uniform, indicating that the CRL could uniformly bear the tensile stress.

3.4. Analysis of the structural stressing state mode

Based on the strain data obtained by extending the NSF method, the stressing state model of the RC beams was established. The strain of a measuring point can represent the stressing state of this point, which leads to the strain of the measuring points of the different cross sections being assembled to cause the stressing state mode of the RC beam into a vector. Then, the S_{strain}-F_j curves are plotted based on the experimental data to analyze the changing characteristics of the stressing state mode and the working performance of the RC beam. The S_{strain}-F_j curve of RC beam BB5 is shown in Figure 8. Among them, the ultimate tensile strain of concrete (ε_y) and yield strain of steel bar (ε'_y) were obtained experimentally.

Before characteristic load P (50 kN) is reached, the strain of the beam increases slowly, and the S_{strain}-F_j curve can be approximately regarded as a straight line, indicat-

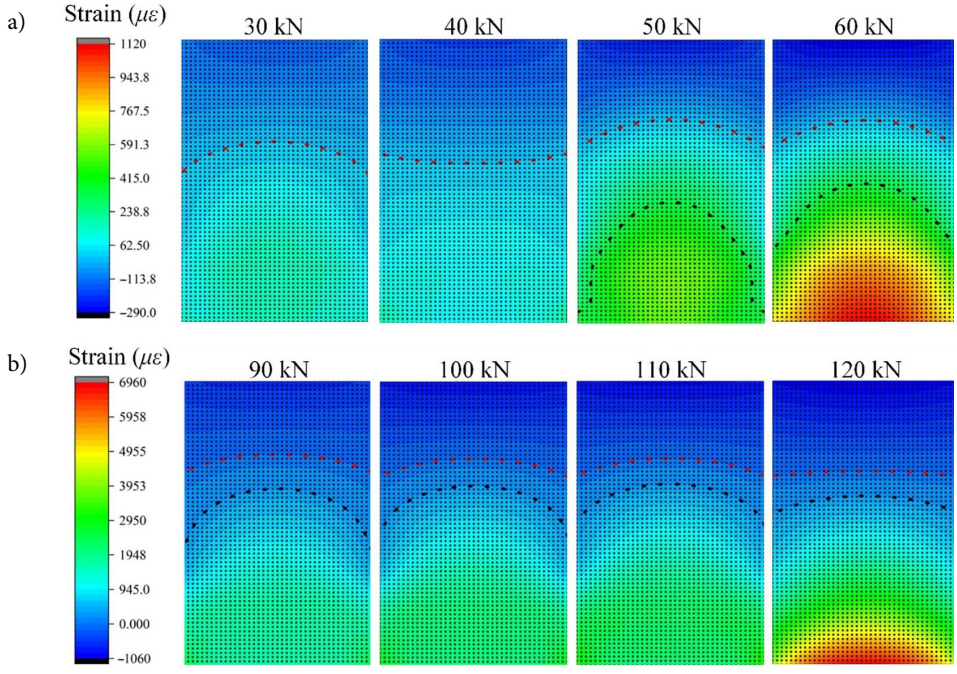

Figure 7. The strain contour maps of BB5: a – The strain contour maps corresponding to the characteristic load P; b – The strain contour maps corresponding to the characteristic load Q

ing that the structural stressing state remains stable. When the load reaches 50 kN, cracks appear at the bottom of the concrete in the mid-span cross section. The tensile strain of concrete gradually reaches the ultimate tensile strain and no longer bears tensile stress. The strain curve of concrete in the compression zone gradually shows a curvilinear distribution. The tension assumed by the concrete at the bottom before cracking is transferred to the steel bar and CRL, which results in a sudden increase in the strain of the steel bar and CRL. Compared with the loading cross section, cracks appear earlier in the mid-span cross section of concrete. Thus, when the load is 50 kN, the strain of longitudinal reinforcement in mid-span cross section suddenly increases, and when the load is 60 kN, the strain of longitudinal reinforcement in bearing cross section suddenly increases.

Beyond the characteristic load Q (110 kN), the strain growth rate of concrete in the tension zone remains stable because the concrete has been damaged. The compressive strain of the concrete in the compression zone increased rapidly until the experimental beam is fractured. Compared with the previous stage, the tensile strain of the FRP grid increases rapidly. The reason may be that after the steel bar reaches the yield load, the tensile force of the steel bar gradually transfers to the FRP grid. In the whole process of the experiment, the strain of the CRL is higher than that of the concrete, and the strain of the FRP grid in the CRL is higher than that of the longitudinal reinforcement, indicating that the CRL plays a significant role in the bearing tensile stress.

The variation trend of the strain at key points of the mid-span cross section of the beam is shown in Figure 9. The leap characteristics of the structural working performance of the beam at characteristic loads P and Q are consistent with the law revealed in Figure 8. At the initial stage of loading, the strain increment of the FRP grid is small, the strain increment increases beyond characteristic load P, and the strain increment beyond characteristic load Q increases suddenly compared with the previous two stages, indicating that the structural stressing state mode has changed at the failure load ascertained by the M-K criterion. Hence, the rationality of the M-K criterion and the stressing state theory was verified by analyzing the strain trends and distribution laws.

4. Experimental study on RC beams strengthened by different CRL schemes

4.1. Investigation into the E_j-F_j curve and in-plane bending moment of the mid-span cross section

According to the NSF method, the GSED values of the different RC beams of the mid-span cross section are plotted in Figure 10 to further investigate the common and different working characteristics. The stressing state of each beam is divided into three stages by the characteristic loads. The lower the GSED value is, the better the stability of the structure. Under the same load, the GSED value of the strengthened beam is less than that of the control beam, indicating that the reinforcement method can improve the stability of the beam. The longer the bond length of the CRL is, the lower the GSED value is, indicating that the bond length of the CRL has a certain effect on the bearing capacity of the strengthened beam. The GSED values of different reinforced RC beams are approximated

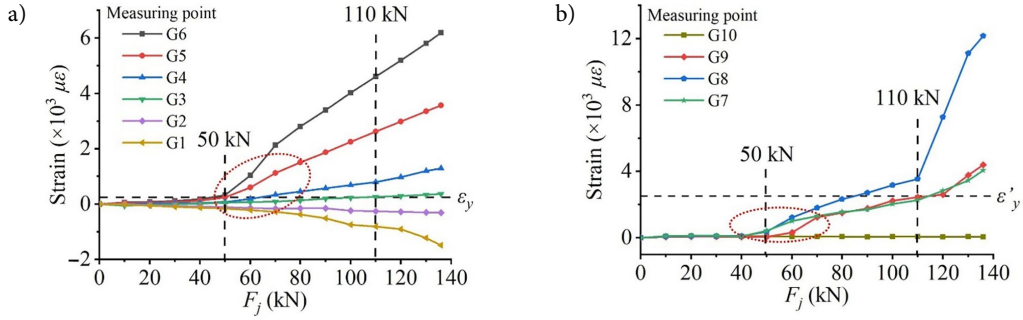

Figure 8. The S_{strain}-F_j curves of RC beam numbered BB5: a – The S_{strain}-F_j curves for the concrete and CRL; b – The S_{strain}-F_j curves for the longitudinal reinforcement and FRP grid

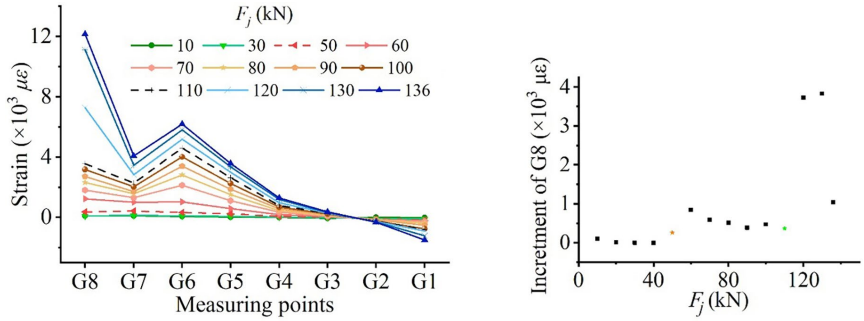

Figure 9. The stressing state of the structure at measuring points of beam numbered BB5

before the characteristic load P is reached. Beyond characteristic load P, the GSED value of the strengthened beam is incrementally smaller than that of the control beam. Beyond characteristic load Q, the GSED value of the reinforced beam is much smaller than that of the unreinforced beam. This result further verifies the reliability of the characteristic load and shows that the effect of the reinforcement method on the structure is mainly concentrated after the characteristic load.

Based on the NSF method, the in-plane bending moment can be obtained, as shown in Figure 10b. Under the same load, the bending moment value of the strengthened beam is smaller than that of the control beam, but the gap is not large, which indicates that the strengthening method has little influence on the bending moment.

4.2. The characteristic points of different schemes

The cracking load of the concrete is close to characteristic load P, and the yield load of the reinforcement is close to the characteristic load Q. The gap between the cracking load and the characteristic point P is less than 10%, and the gap between the yield load and the characteristic load Q is less than 6%. Hence, based on the stressing state of the beam, the elastic stage is determined from the initial load to characteristic load P, the elastic-plastic stage is determined from the characteristic load P to characteristic load Q, and the failure stage is beyond the characteristic load Q.

The loads of the beam at different stages are shown in Figure 11a. Beams bonded with CRL are able to accommodate more load during the elastic stage. With an increase in the thickness of the FRP grid and the fiber content, the strengthened beams are able to endure more loads during the elastic-plastic stage, which indicates that the thickness of the FRP grid has a certain influence on the elastic-plastic stage of the beam. With a reduction in the bond length of the CRL, the load that the strengthened beam can bear in the elastic stage decreases, indicating that the influence of the bond length of the CRL of the beam in the elastic stage is greater than that in other stages. In summary, the bond length of the CRL, the thickness of the FRP grid and the fiber content in the CRL can be used to increase the ultimate bearing capacity of the experimental beam by increasing the load that can be borne in the elastic stage or elastic-plastic stage.

The proportions of the different loading stages during the test are shown in Figure 11b. Compared to control beam BB0, strengthened beams have a greater proportion of the elastic stage in the overall loading process. The failure stage of the strengthened beam accounts for a relatively small percentage of the overall loading process.

4.3. Investigation into the characteristics of strain fields

To further investigate the effect of the strengthening method, the strain contour map of the beam is shown in Figure 12, and the strain contour maps of the experimental beams BB6 and BB0 are compared. At the initial loading stage, the strain distribution of the test beam is approximate, indicating that the strengthening method has little

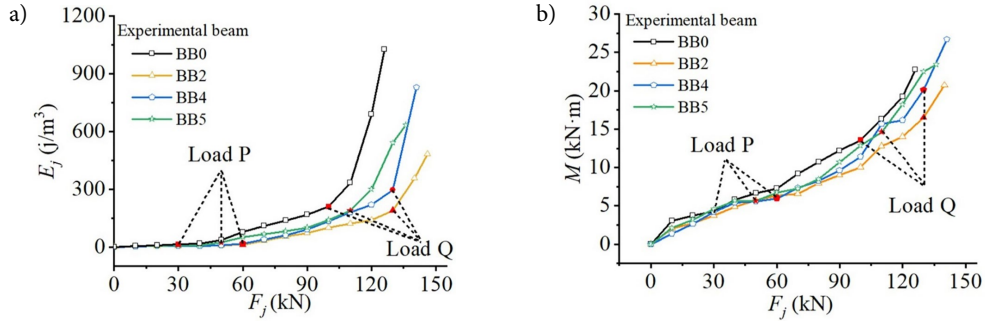

Figure 10. The E_j-F_j curves and in-plane bending moment with different beams of the mid-span cross section: a – The E_j-F_j curve; b – The in-plane bending moment

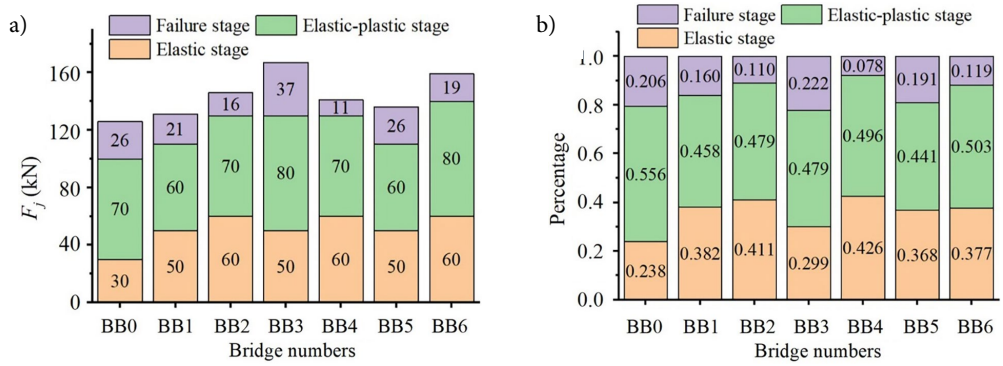

Figure 11. Three stages in the test: a – Loads at different stages; b – The proportion of the different loading stages

influence on the strain distribution of the test beam in the elastic stage. The crack area of the control beam appears earlier than in the strengthened beam. In the elastic-plastic stage and failure stage, the maximum tensile strain of the beam BB0 is mainly concentrated in the reinforcement area, while the maximum tensile strain of the beam BB6 is mainly concentrated in the CRL area. In summary, the reinforcement method could change the distribution of the tensile strain in the elastic-plastic and failure stages of the structure.

The strain of the longitudinal reinforcement at the mid-span cross section is analyzed, as shown in Figure 13. Among them, ε_P represents the reinforcement strain of the experimental beam BB0 when it reaches characteristic load P, and ε_Q represents the reinforcement strain of the experimental beam BB0 when it reaches characteristic load Q. The influence of the thickness of the FRP grid on the strain of the reinforcement is studied, as shown in Figure 13a. In the elastic stage, the strain of the reinforcement is small, and the reinforcement strain of the strengthened beam is close to that of the control beam. In the elastic-plastic stage, the strain of the reinforcement increases rapidly. Since the CRL could assist the reinforcement in bearing tensile force, the reinforcement strain of the strengthened beam under the same load is less than the strain of the control beam. At this point, due to the different thicknesses of the FRP grid, the reinforcement strain is different. In the failure stage, the strain of the reinforcement increases rapidly compared with that in the previous stage, and the reinforcement strain value of the control beam is much higher than that of the strengthened beam.

The influence of the CRL bonding length and fiber content on the steel bar strain is shown in Figure 13b and 13c. Here, the shorter the bond length of the CRL is, the greater the final strain value of the reinforcement, but the

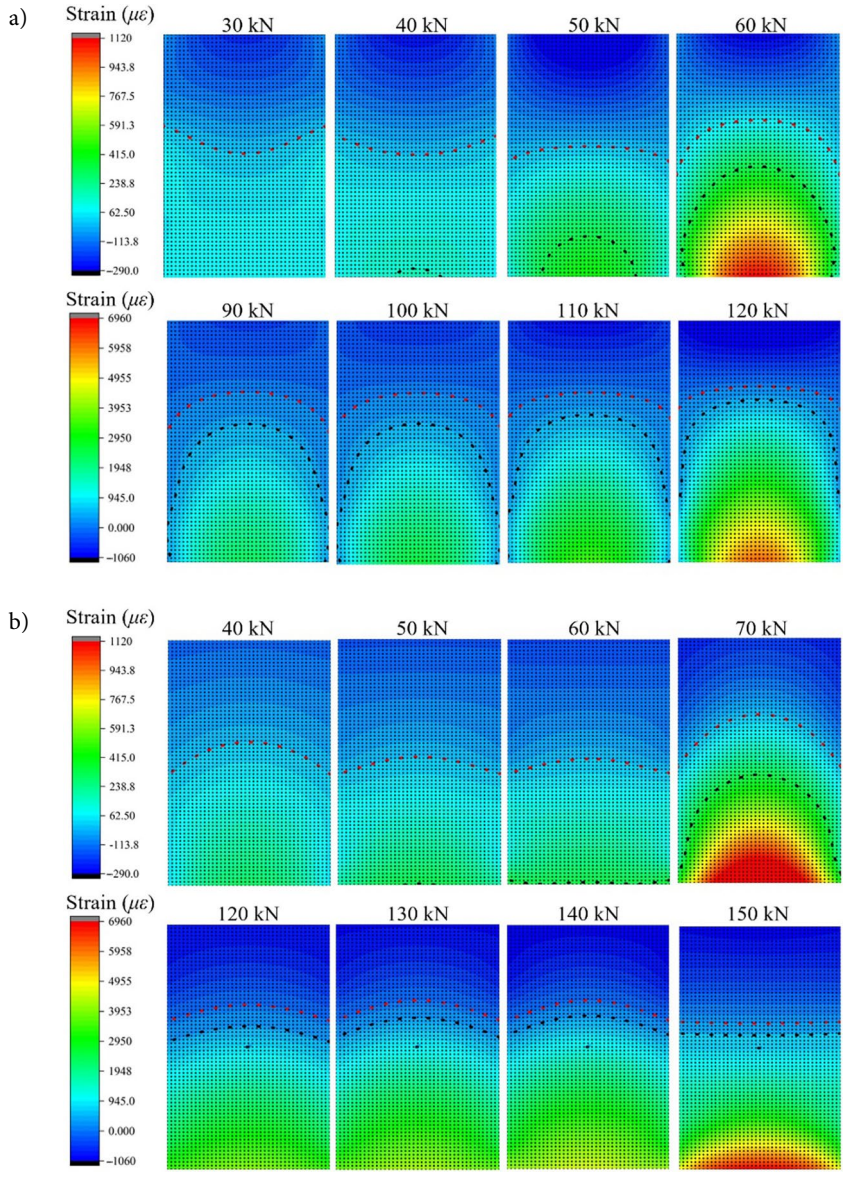

Figure 12. The strain contour maps: a – Beam numbered BB0; b – Beam numbered BB6

fiber content has little influence on the final strain. In conclusion, the method proposed in this paper could reduce the tensile stress of steel reinforcements in the elastic-plastic stage and failure stage due to the partial tensile stress borne by the CRL.

Figure 14 shows the strain modes at the mid-span cross section of experimental beams with different bond length of CRL. By comparing the compressive strain of different experimental beams, the strengthening method has little effect on concrete strain in compression zone. During the whole loading process, the tensile strain of the concrete of the beam BB0 is much smaller than that of the reinforcing steel. Compared with the experimental beam BB0, the tensile strain of the concrete of the other experimental beams increasees and the strain of the steel bars decrease. When the experimental beam numbered BB2, BB4 and BB6 entered the elastic-plastic stage, the strain of CRL increased rapidly, and the strain corresponding to the breaking load was greater than that of the reinforcement. With the reduction of the bond length of CRL, the gap between the strain of reinforcement and the strain of concrete measuring point G5 decreases. The effects of strengthening method on the strain of concrete and reinforcement mainly concentrated in the elastic-plastic stage and the failure stage.

4.4. Investigation into the structural deformation of the experimental beams

The effects of the strengthening schemes on structural deformation are studied, as shown in Figure 15. Here, d_P and d_Q represent the vertical displacement of the experimental beam BB0 when it reaches characteristic load P and characteristic load Q, respectively, and d_F represents the vertical displacement of the beam numbered BB1 when it reaches the breaking load.

The vertical deformation of the experimental beams numbered BB0, BB1, BB2 and BB3 is investigated, as shown in Figure 15a. In the elastic stage, the vertical dis-

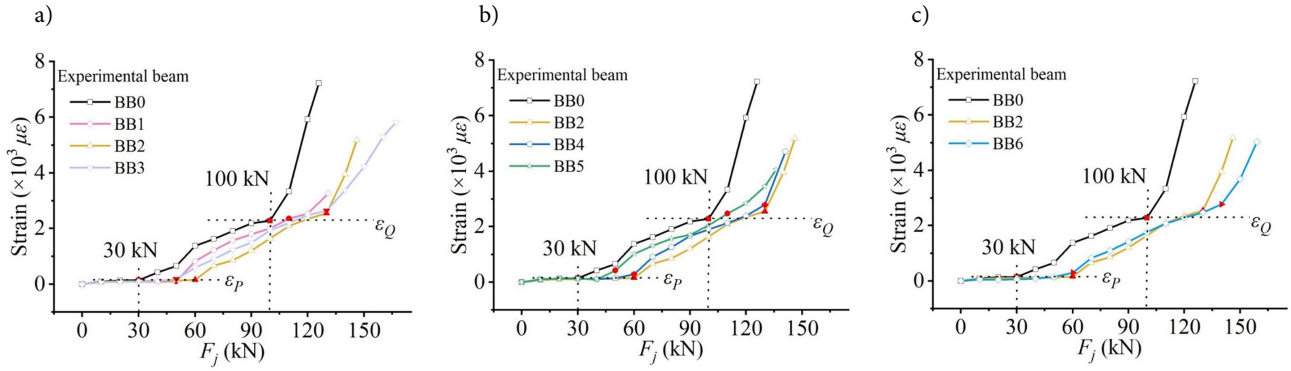

Figure 13. Strain of reinforcement in different experimental beams: a – Experimental beams with different thicknesses of FRP grid; b – Experimental beams with different bond lengths of CRL; c – Experimental beams with different fiber contents

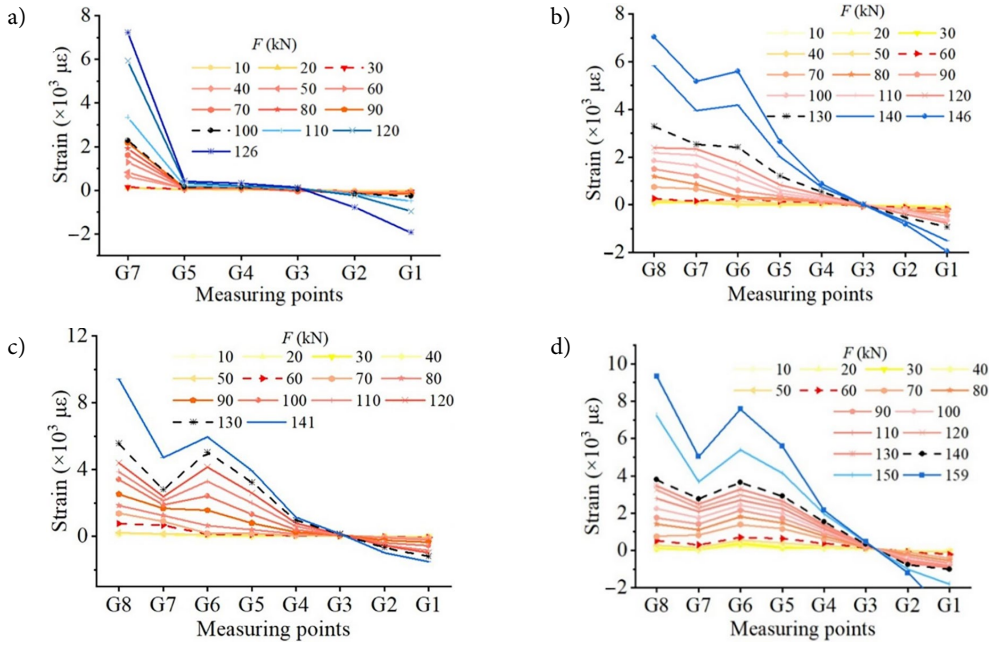

Figure 14. Strain of mid-span cross section in different experimental beams: a – Experimental beam numbered BB0; b – Experimental beam numbered BB2; c – Experimental beam numbered BB4; d – Experimental beam numbered BB6

placement increases slowly, and the deformation of the strengthened beam is close to that of the unreinforced beam, which indicates that the strengthening method has little effect on the deformation. In the elastic-plastic stage, the vertical displacement growth rate of the experimental beams increases, and the growth rate of different experimental beams are different. Under the same load, the deformation of all strengthened beams is less than that of the control beam, indicating that the method could restrain the deformation of the beam in the elastic-plastic stage. Although the displacement of the beams increased at different rates, the vertical deformation of the beams was close to each other when the experimental beams reached the yield load. In the failure stage, the vertical displacement increases rapidly compared to the previous stage, and the deformation of the strengthened beam is much smaller than that of the control beam during the whole failure stage. Under the same load, as the thickness of the FRP grid increases, the vertical deformation of the beam decreases. When the experimental beams reach the breaking load, the vertical deformation of the strengthened beams is similar and much smaller than that of the control beam.

The vertical deformation of other experimental beams is shown in Figure 15b and 15c. Under the same load, the

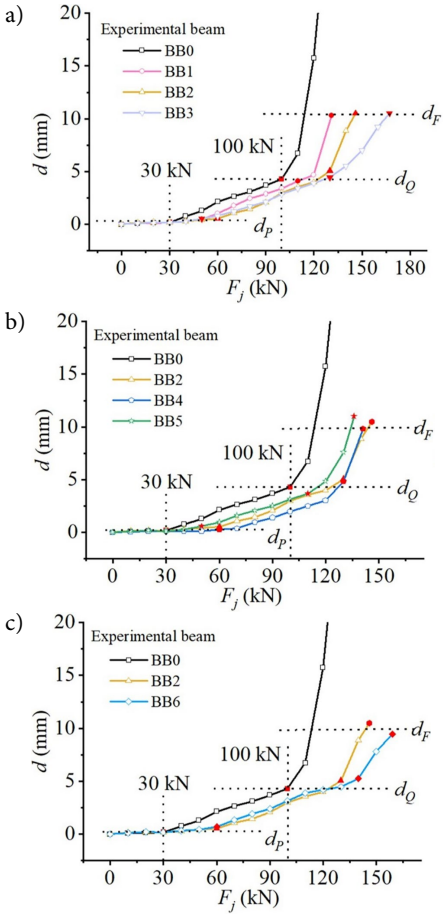

Figure 15. The vertical displacement of different experimental beams: a – The experimental beams with different thicknesses of the FRP grid; b – The experimental beams with different bond lengths of the CRL; c – The experimental beams with different fiber contents

method adopted in this paper could reduce the vertical deformation of the beam in the elastic-plastic stage and the failure stage, especially in the failure stage. The final vertical deformation of the strengthened beam is significantly lower than that of the control beam. The thickness of the FRP grid, bond length of the CRL and fiber content have little influence on the final vertical deformation of the beam.

Conclusions

The flexural tests of RC beams bonded with FRP grids and ECC materials were carried out, and the GSED parameters were constructed based on the structural stressing state theory and NSF method. Using the M-K criterion tool, the leap characteristics of the strengthened RC beams were revealed, and the hidden mechanical properties under different strengthening conditions were reflected. The main conclusions are as follows:

(1) The damage mode of the control set is typical concrete damage, and the damage mode of the strengthened beam is mainly FRP fracture. The ultimate load of RC beams strengthened with CRL is significantly improved compared to control beams and increases with the increase of bond length of CRL, fiber content in ECC and FRP thickness.

(2) The $E_{j,norm}$-F_j curve is constructed using the structural stressing state theory, and the M-K criterion is used to identify the leap characteristics (characteristic loads P and Q) of the structure from the stable state to the unstable state. The essential changes of the structural stress state are revealed, and the loading process is divided into the elastic stage and the elastic-plastic stage as well as the failure stage.

(3) The analysis of deformation, strain of different materials and the trend of GSED further reveals the abrupt change characteristics at the characteristic load. The experimental strain data do not reflect the working characteristics of the overall structure, so the NSF method is introduced to give the strain fields at critical sections. The method directly reflects the stress state characteristics of beams under different loads, highlights the variation at the characteristic loads, and further verifies the reliability of the M-K criterion.

(4) Different influencing factors have different effects on different loading stages of the beam. The longer the bond length of CRL the higher the characteristic load P. The higher the FRP thickness and fiber content the higher the characteristic load Q. Compared to unreinforced beam, the reinforced beam has less vertical deformation in the elastic-plastic and failure stages.

Acknowledgements

The authors would like to thank the members of the CSU 1004 office for their selfless help and useful suggestions.

Funding

This work was financially supported by the National Natural Science Foundation of China (Grant Nos. 52008399).

Author contributions

Guorui Sun and Yuzhou Zheng conceived the study and were responsible for the design and development of the data analysis. Jie Lai and Yuzhou Zheng were responsible for data collection and analysis. Kaikai Zheng and Jun Shi were responsible for data interpretation. Guorui Sun wrote the first draft of the article.

Disclosure statement

The authors declare no conflict of interest.

References

Afefy, H. M., Kassem, N., & Hussein, M. (2015). Enhancement of flexural behaviour of CFRP-strengthened reinforced concrete beams using engineered cementitious composites transition layer. *Structure and Infrastructure Engineering*, *11*(8), 1042–1053. https://doi.org/10.1080/15732479.2014.930497

Al-Salloum, Y. A., Siddiqui, N. A., Elsanadedy, H. M., Abadel A. A., & Aqel M. A. (2011). Textile-reinforced mortar versus FRP as strengthening material for seismically deficient RC beam-column joints. *Journal of Composites for Construction*, *15*, 920–933. https://doi.org/10.1061/(ASCE)CC.1943-5614.0000222

Dai, J. G., Munir, S., & Ding, Z. (2014). Comparative study of different cement-based inorganic pastes towards the development of FRP strengthening technology. *Journal of Composites for Construction*, *18*(3), A4013011. https://doi.org/10.1061/(ASCE)CC.1943-5614.0000420

Escrig, C., Gil, L., Bernat-Maso, E., & Puigvert, F. (2015). Experimental and analytical study of reinforced concrete beams shear strengthened with different types of textile-reinforced mortar. *Construction and Building Materials*, *83*, 248–260. https://doi.org/10.1016/j.conbuildmat.2015.03.013

Ge, W. J., Ashour, A. F., Ji, X., Cai, C., & Cao, D. F. (2017). Flexural behavior of ECC-concrete composite beams reinforced with steel bars. *Construction and Building Materials*, *159*, 175–188. https://doi.org/10.1016/j.conbuildmat.2017.10.101

Ge, W. J., Ashour, A. F., Cao, D., Lu W., Gao, P., Yu, J., Ji, X., & Cai, C. (2019). Experimental study on flexural behavior of ECC-concrete composite beams reinforced with FRP bars. *Composite Structures*, *208*, 454–465. https://doi.org/10.1016/j.compstruct.2018.10.026

Godat, A., Hammad, F., & Chaallal, O. (2020). State-of-the-art review of anchored FRP shear-strengthened RC beams: A study of influencing factors. *Composite Structures*, *254*, 112767. https://doi.org/10.1016/j.compstruct.2020.112767

He, W., Wang, X., & Wu, Z. (2020). Flexural behavior of RC beams strengthened with prestressed and non-prestressed BFRP grids. *Composite Structures*, *246*, 112381. https://doi.org/10.1016/j.compstruct.2020.112381

Huang, Y., Zhang, Y., Ming, Z., & Zhou, G. (2014). Method for predicting the failure load of masonry wall panels based on generalized strain-energy density. *Journal of Engineering Mechanics*, *140*(8), 04014061. https://doi.org/10.1061/(ASCE)EM.1943-7889.0000771

Kadhim, A. M., Numan, H. A., & Özakça, M. (2019). Flexural strengthening and rehabilitation of reinforced concrete beam using BFRP composites: Finite element approach. *Advances in Civil Engineering*, *2019*, 4981750. https://doi.org/10.1155/2019/4981750

Kara, I. F., Ashour, A. F., & Köroğlu, M. A. (2015). Flexural behavior of hybrid FRP/steel reinforced concrete beams. *Composite Structures*, *129*, 111–121. https://doi.org/10.1016/j.compstruct.2015.03.073

Kendall, M. G., & Gibbons, J. D. (1990). *Rank correlation methods* (5th ed.). Edward Arnold.

Li, D., Zhou, J. L., & Ou, J. P. (2020). Damage, nondestructive evaluation and rehabilitation of FRP composite-RC structure: A review. *Construction and Building Materials*, *271*, 121551. https://doi.org/10.1016/j.conbuildmat.2020.121551

Xiao, H. H., Luo, L., Shi, J., Jiang, H. C., & Wu Z. W. (2021). Stressing state analysis of multi-span continuous steel-concrete composite box girder. *Engineering Structures*, *246*, 113070. https://doi.org/10.1016/j.engstruct.2021.113070

Mann, H. B. (1945). Nonparametric tests against trend. *Econometrica*, *13*, 245–259. https://doi.org/10.2307/1907187

Ma, H., Yi, C., & Wu, C. (2021). Review and outlook on durability of engineered cementitious composite (ECC). *Construction and Building Materials*, *287*(2), 122719. https://doi.org/10.1016/j.conbuildmat.2021.122719

Shanmugasundaram, N., & Praveenkumar, S. (2021). Influence of supplementary cementitious materials, curing conditions and mixing ratios on fresh and mechanical properties of engineered cementitious composites-A review. *Construction and Building Materials*, *309*(22), 125038. https://doi.org/10.1016/j.conbuildmat.2021.125038

Shi, J., Zheng, K. K., Tan, Y. Q., Yang K. K., & Zhou, G. C. (2019). Response simulating interpolation methods for expanding experimental data based on numerical shape functions. *Computers and Structures*, *218*, 1–8. http://doi.org/10.1016/j.compstruc.2019.04.004

Sogut, S., Dirar, S., Theofanous, M., Faramarzi, A., & Nayak, A. N. (2021). Effect of transverse and longitudinal reinforcement ratios on the behaviour of RC T-beams shear-strengthened with embedded FRP BARS. *Composite Structures*, *262*(5), 113622. http://doi.org/10.1016/j.compstruct.2021.113622

Yao, J., Teng, J. G., & Chen, J. F. (2005). Experimental study on FRP-to-concrete bonded joints. *Composites Part B: Engineering*, *36*(2), 99–113. https://doi.org/10.1016/j.compositesb.2004.06.001

Yuan, W. Y., Han, Q., Bai, Y. L., Du, X. L., & Yan, Z. W. (2021). Compressive behavior and modelling of engineered cementitious composite (ECC) confined with LRS FRP and conventional FRP. *Composite Structures*, *272*(15), 114200. https://doi.org/10.1016/j.compstruct.2021.114200

Zheng, Y. Z, & Wang, W. W. (2015). Tensile behaviour of FRP grid strengthening ECC composite under a uniaxial loading. In *Second International Conference on Performance-based and Lifecycle Structural Engineering* (pp. 529–535), Brisbane, Australia. https://doi.org/10.14264/uql.2016.1149

Zheng, Y. Z., Wang, W. W., & Brigham, J. C. (2016). Flexural behaviour of reinforced concrete beams strengthened with a composite reinforcement layer: BFRP grid and ECC. *Construction and Building Materials*, *115*, 424–437. https://doi.org/10.1016/j.conbuildmat.2016.04.038

Zheng, Y. Z., Zhang, L. F., & Xia, L. P. (2018). Investigation of the behaviour of flexible and ductile ECC link slab reinforced with FRP. *Construction and Building Materials*, *166*, 694–711. https://doi.org/10.1016/j.conbuildmat.2018.01.188